Enhanced marine biological pump as a trigger for the onset of the late Paleozoic ice age

Feifei Zhang, Alexandre Pohl, Maya Elrick, Guang-Yi Wei, Keyi Cheng, Peter Crockford, Mojtaba Fakhraee, Yi-Bo Lin, Na Li, Xiang-Dong Wang, et al.

GEOLOGY

Enhanced marine biological pump as a trigger for the onset of the late Paleozoic ice age

Feifei Zhang[1]*, Alexandre Pohl[2], Maya Elrick[3], Guang-Yi Wei[1], Keyi Cheng[4], Peter Crockford[5], Mojtaba Fakhraee[6], Yi-Bo Lin[1], Na Li[1], Xiang-dong Wang[1], Shu-zhong Shen[1]

The mid-Tournaisian carbon isotope excursion (TICE) represents the largest positive carbon isotope excursion in the late Paleozoic, coinciding with the onset of the late Paleozoic ice age (LPIA). Here, to investigate changes in the marine biological pump during the TICE, we measured barium isotopes (δ^{138}Ba) in two marine limestone sections in the Antler foreland basin (USA). We found the largest positive δ^{138}Ba shifts recorded in geological history, indicating increased marine export productivity in the Antler foreland basin, followed by the productivity-driven expansion of anoxia. The nearly identical stratigraphic trends, along with different absolute values in δ^{138}Ba between the two sites, suggest spatial differences in marine biological pump intensity during the Early Mississippian. Earth system model simulations indicate that a global increase of 30% in marine export productivity is needed to explain observed changes. Our findings support the idea that an enhanced marine biological pump contributed to elevated organic carbon burial and the transition from a greenhouse climate to the LPIA.

INTRODUCTION

The transition from the middle Paleozoic "greenhouse" to the late Paleozoic "icehouse" during the Early Mississippian is one of the most notable climatic changes in Earth's history, yet its causes remain unclear (*1*–*3*). While the precise timing of this transition is debated on the basis of an extended cooling period, it has been argued that it was temporally linked to a pronounced positive carbonate carbon isotope ($\delta^{13}C_{carb}$) excursion of up to +7‰ (per mil), referred to as the mid-Tournaisian carbon isotope excursion (TICE) (*1*, *2*, *4*–*6*). The TICE represents one of the largest positive carbon isotope excursions during the Phanerozoic and has been reported from localities all over the globe (*1*, *2*, *4*, *5*, *7*) and has spanned ~4 million years (Myr) (*4*, *6*, *8*). Marine biodiversity during the TICE interval, based on data from South China and the global Mississippian reef database, is evidenced to be among the lowest of the middle to late Paleozoic and is comparable to levels recorded after the end-Permian mass extinction (*9*, *10*).

It has been suggested that the TICE was driven by an increase in the burial of organic carbon, which led to a reduction in atmospheric CO_2 concentration (pCO_2) levels and caused global climatic cooling (*1*, *4*, *7*, *8*), initiating the late Paleozoic ice age (LPIA) (*2*, *11*). However, the exact trigger for an increase in organic carbon burial remains poorly understood, and there is ongoing debate about how to interpret carbon isotope signatures at that scale in the sedimentary record (*12*, *13*). Many prior studies have invoked increased marine productivity in the Early Mississippian oceans to drive organic carbon burial and TICE development (*5*, *14*–*16*). For example, carbon and nitrogen isotope results from previous works have been interpreted to be the result of an intensification of marine productivity in the Early Mississippian (*5*, *15*). Zinc isotope (δ^{66}Zn) records from two TICE sections in South China indicate that marine primary productivity played a critical role in driving the carbon isotope excursion during the TICE event; however, reported increases in δ^{66}Zn values are significantly delayed from the onset of the positive carbon isotope excursion (*17*). Uranium isotopes have also been used to propose an expansion of Early Mississippian marine anoxia/euxinia as a result of enhanced marine productivity, leading to enhanced organic carbon burial (*8*). A plausible chain of events leading to climatic cooling may have involved increased carbon export fluxes to deep waters due to enhanced marine productivity and/or improved organic matter preservation from expanded anoxia, which fostered a significant positive carbonate carbon isotope excursion. This process would subsequently have consumed atmospheric CO_2 and resulted in a decrease in global temperatures. Despite the potentially critical role of marine productivity in driving the TICE, Early Mississippian marine anoxia, climatic cooling, and the subsequent low marine biodiversity, direct evidence for enhanced marine productivity in the Early Mississippian oceans remains absent.

Barium isotope variations (δ^{138}Ba) in marine carbonates are an emerging proxy to place direct constraints on marine export productivity (i.e., marine biological pump) in both modern and ancient oceans (*18*–*20*). This is because (i) the modern distribution of dissolved Ba (hereafter $[Ba]_{diss}$) shows a pattern similar to major nutrients such as silicon and (ii) the particulate Ba accumulation rate in certain regions has been shown to positively correlate with the downward flux of organic carbon (*21*–*24*). The vertical distribution of seawater $[Ba]_{diss}$ and its isotopes depends on the precipitation of pelagic barites through microbial remineralization of sinking organic matter and the partial dissolution of barite particles at depth associated with microbial sulfate reduction (fig. S1) (*24*–*28*). Barite precipitation from seawater is associated with a relatively large isotopic fractionation, resulting in barite crystals enriched in the light isotope ($\delta^{138}Ba_{barite\text{-}diss} = \delta^{138}Ba_{barite} - \delta^{138}Ba_{diss} \approx -0.5‰ - -0.4‰$, where $\delta^{138}Ba_{diss}$ denotes the isotopic composition of $[Ba]_{diss}$ in seawater) (*27*, *29*, *30*). In contrast, barite dissolution is associated with a limited isotopic fractionation (*18*, *24*, *27*, *30*). As a result, during periods of an increased marine biological pump, enhanced carbon export would pump more Ba from the surface to deep waters, decreasing the $[Ba]_{diss}$ in surface waters and shifting the $\delta^{138}Ba_{diss}$ of those regional

[1]State Key Laboratory of Critical Earth Material Cycling and Mineral Deposits, School of Earth Sciences and Engineering, and Frontiers Science Center for Critical Earth Material Cycling, Nanjing University, Nanjing 210023, China. [2]Biogéosciences UMR 6282, Université Bourgogne Europe, CNRS, F-21000 Dijon, France. [3]Department of Earth & Planetary Sciences, University of New Mexico, Albuquerque, NM 87131, USA. [4]Department of Earth and Environmental Sciences, Michigan State University, East Lansing, MI 48824, USA. [5]Department of Earth Sciences, Carleton University, Ottawa, ON K1S5B6, Canada. [6]Department of Earth and Planetary Sciences, Yale University, New Haven, CT 06520, USA.
*Corresponding author. Email: fzhang@nju.edu.cn

waters to higher values. This phenomenon has been observed in multiple localities in the modern South Atlantic Ocean (*26*) and northern South China Sea (*31*). The residence time of Ba in modern seawater is comparable to the scale of ocean mixing, implying that the Ba isotope proxy is a basinal rather than a global paleoceanographic proxy (*24*). Although the Ba isotope fractionation during carbonate precipitation remains less well constrained, existing studies suggest that the Ba isotope fractionation during aragonite ($BaCO_3$) precipitation is a function of growth rate, while fractionation during calcite and witherite precipitation displays a negligible fractionation (*32*–*35*). For example, laboratory experiments on witherite dissolution and precipitation demonstrate that the Ba isotope fractionation between witherite and aqueous fluid under isotopic equilibrium is close to 0‰ (*32*). Therefore, when properly screening for diagenesis and evaluating changes in carbonate mineralogy, well-preserved marine limestone samples can record the δ^{138}Ba signals of ancient seawater and be used to shed light on past regional changes to the marine biological pump.

To obtain constraints on the extent of changes in the marine biological pump in Early Mississippian oceans and to constrain potential drivers of the profound climate changes and carbon cycle perturbations at this time, we document the first δ^{138}Ba isotope trends across the TICE from two widely separated (by ~1300 km) and well-studied sections (Fig. 1): the Pahranagat Range (PR) section in southern Nevada (number of samples = 47) and the Sacagawea Peak (SP) section in southwest Montana (number of samples = 30), USA. We then use a global, spatially resolved Earth system model of intermediate complexity [cGENIE; (*36*)] to simulate the biogeochemical landscape in Early Mississippian oceans. Through the combination of geochemical proxy data and model simulations, we establish clear links between the marine biological pump, global climate, marine redox chemistry, and low marine biodiversity during this critical climate transition.

RESULTS

We correlate the SP and PR sections via established high-resolution δ^{13}C chemostratigraphy and biostratigraphy. In both study sections, we observed a large positive shift in the barium isotope values (δ^{138}Ba). Specifically, the δ^{138}Ba values from the PR section range from −0.15 to 1.12‰ (Fig. 2), which span the entire range of values previously reported for geological samples and represent the largest positive excursion ever documented. $\delta^{13}C_{carb}$ values range from 0.31 to 7.06‰, and the trends match those reported by Maharjan *et al.* (*6*) and Cheng *et al.* (*8*), representing the largest positive carbon isotope excursion during the late Paleozoic. The stratigraphic variations in δ^{138}Ba from the PR section can be subdivided into four stages (Fig. 2). Stage I exhibits a large positive δ^{138}Ba shift from −0.15 to 0.68‰ that corresponds to the rising limb of the $\delta^{13}C_{carb}$ excursion. In stage II, δ^{138}Ba exhibits a large negative shift from 0.68 to −0.08‰, when $\delta^{13}C_{carb}$ shows a large positive excursion to its first peak of 7‰, followed by the onset of a brief ~3‰ negative shift (Fig. 2). In stage III, δ^{138}Ba trends exhibit another large positive shift from −0.08 to 1.12‰, when $\delta^{13}C_{carb}$ displays a brief nadir, followed by a second positive shift. Last, in stage IV, δ^{138}Ba remains at high values with a mild declining trend when $\delta^{13}C_{carb}$ values gradually decrease to pre-TICE values.

In contrast, although the δ^{138}Ba values from the SP section yielded similar four-stage variations to the PR section (Fig. 2), the overall variations are of lower magnitude, with respect to the δ^{138}Ba value. Specifically, stage I in the SP section shows a positive shift from −0.08 to 0.20‰. In stage II, the δ^{138}Ba values decline from 0.20 to −0.23‰ (Fig. 2). Stage III records another positive shift, from −0.23 to 0.17‰; however, it is important to note that this excursion is represented by only a few data points. In stage IV, δ^{138}Ba values remain comparatively stable, fluctuating between 0.00 and 0.27‰ (Fig. 2).

DISCUSSION

Evaluating the primary seawater signals of δ^{138}Ba records

Several lines of evidence support the interpretation that our δ^{138}Ba data represent a primary seawater signal, reflecting secular variations in δ^{138}Ba within the Early Mississippian Antler foreland basin, rather than an artifact related to local diagenetic or depositional processes. Given the relatively high concentration of Ba in the upper continental crust [UCC; ~600 parts per million (ppm)] (*37*), detrital Ba contamination, which may occur during deposition, diagenesis, or sample dissolution, could potentially influence δ^{138}Ba values. We evaluate these scenarios by estimating the proportion of carbonate-hosted Ba (f_{carb}; no unit, values ranging from 0 to 1), the carbonate-hosted Ba content (Ba_{carb}; in parts per million), and the carbonate-hosted Ba isotopic composition ($\delta^{138}Ba_{carb}$; in per mil)

$$f_{carb} = 1 - (Ba/Al)_{detrital} \times (Ba/Al)_{sample} \quad (1)$$

$$Ba_{carb} = Ba_{sample} - (Ba/Al)_{detrital} \times Al_{sample} \quad (2)$$

$$\delta^{138}Ba_{carb} = \left[\delta^{138}Ba_{sample} - \delta^{138}Ba_{detrital} \times \left(1 - f_{carb}\right)\right] / f_{carb} \quad (3)$$

Following the approaches of Wei *et al.* (*19*) and Bridgestock *et al.* (*18*), we set $\delta^{138}Ba_{detrital} = \delta^{138}Ba_{UCC} = 0.00‰$ (*38*) and $(Ba/Al)_{detrital} = 0.0037$ (*18*, *39*). The calculated values of f_{carb}, Ba_{carb}, and $\delta^{138}Ba_{carb}$ are presented in figs. S2 and S3. Except for one sample with an f_{carb} value of 0.5, the estimated f_{carb} values for the PR section vary between 0.80 and 0.99, with a median of 0.92. These values indicate that, on average, less than 8% of Ba in our study samples appears to be related to detrital or sample preparation contamination. In the SP section, f_{carb} values range from 0.49 to 0.97, with a median value of 0.92. Furthermore, the stratigraphic trends of $\delta^{138}Ba_{carb}$ and $\delta^{138}Ba_{sample}$ are nearly identical (figs. S2 and S3), suggesting that the observed δ^{138}Ba trends are not the result of detrital or sample preparation Ba contamination.

We compared our δ^{138}Ba data with standard carbonate geochemical tracers, such as Mn and Sr contents, Mn/Sr ratios, and δ^{18}O compositions, to evaluate potential diagenetic influences. Although these geochemical proxies are not specifically designed for carbonate Ba isotope studies, they are useful for identifying largely altered samples. Meteoric diagenesis typically decreases both δ^{13}C and δ^{18}O values of carbonate sediments (*40*). Except for two samples with relatively low δ^{18}O values of −8.56 and −8.40‰ (shown in gray in Fig. 2), the δ^{18}O values for the PR section range from −2.95 to −5.97‰, with a median of −3.68. These results are indicative of a limited influence from meteoric diagenesis (*41*, *42*). In the SP section, two samples have δ^{18}O values lower than −8‰ (shown in gray in Fig. 2), while the remaining samples vary between −3.19 and −6.56‰, with a median of −4.86‰. Cross-plots of δ^{138}Ba versus δ^{18}O show no statistically significant correlations [PR section: correlation coefficient (r) = 0.31 and P = 0.04; SP section: r = 0.13 and

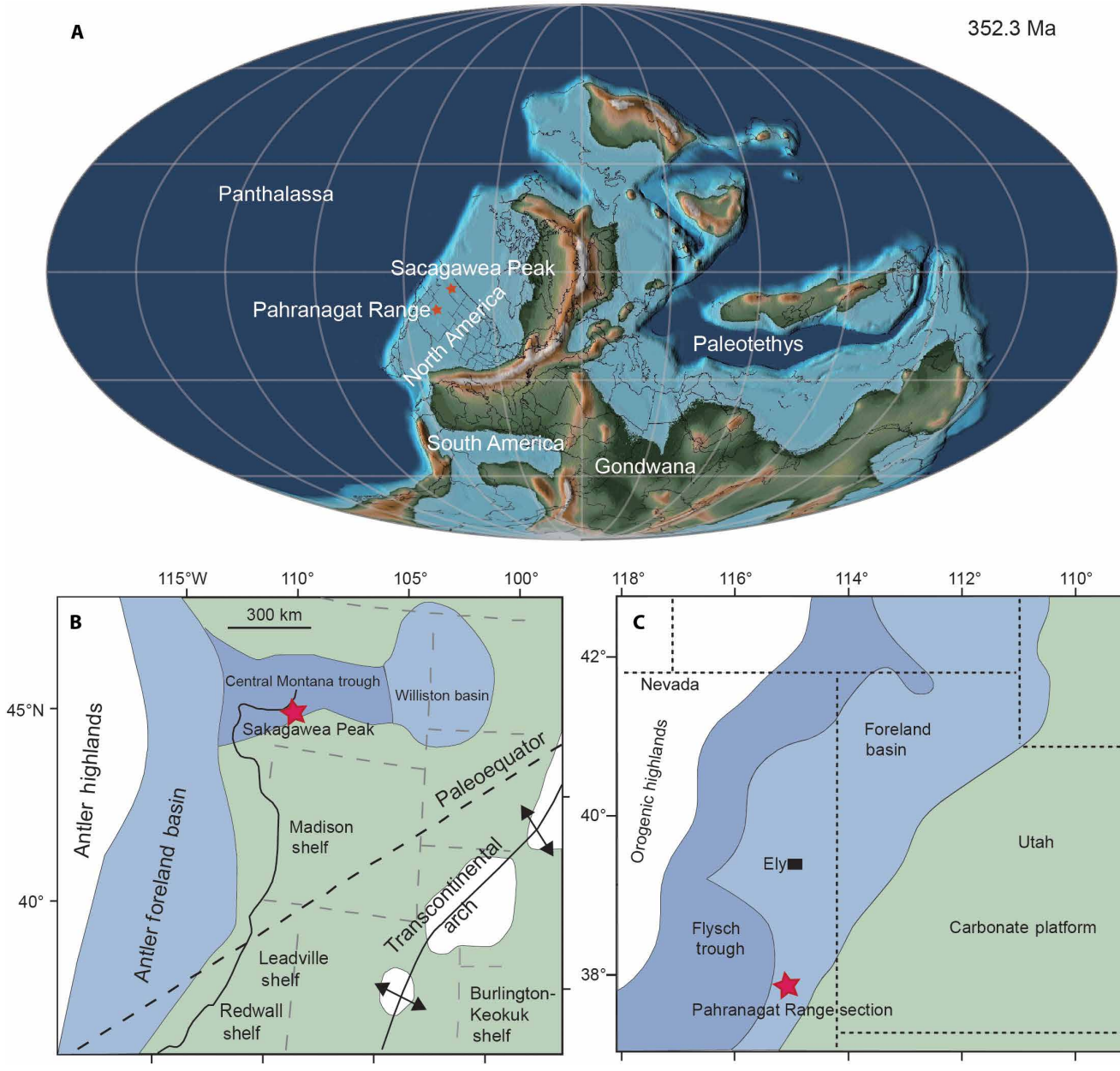

Fig. 1. The geological localities of our two study sections. (**A**) Early Mississippian paleogeography of North America, modified from Scotese and Wright (*69*) (https://creativecommons.org/licenses/by/4.0/). The red stars indicate the locations of the study areas in the present-day. (**B** and **C**) General paleogeographic reconstruction of the Antler foreland basin during the Early Mississippian (*6*, *8*) showing the localities of SP (B) and PR (C).

$P = 0.57$]. $\delta^{13}C$ values are strongly positive for both sections, indicating limited to no influence from meteoric diagenesis on our study carbonates.

Burial diagenesis tends to decrease Sr content, increase Mn content, and thus increase the Mn/Sr ratio of carbonate sediments (*43*). A Mn/Sr ratio between 1 and 10 is suggested as a basic benchmark for indicating preservation of primary seawater signatures in ancient carbonate rocks (*43*). In the PR samples, Mn and Sr contents range between 14 ppm and 142 ppm (median: 40 ppm) and between 471 ppm and 1260 ppm (median: 889 ppm), respectively (see fig. S4). In the SP section, Mn and Sr contents range from 11 ppm to 175 ppm (median: 39 ppm) and from 61 ppm to 1083 ppm (median: 443 ppm), respectively (see fig. S5). Together these results present the Mn/Sr ratio of the SP and PR samples to be between 0.02 and 0.28 with a median value of 0.04 and between 0.04 and 0.61 with a median value of 0.11, respectively. These values are well below the traditional thresholds for carbonate sediments altered by burial diagenesis, suggesting potential preservation of original seawater $\delta^{138}Ba$ trends in the Antler foreland basin. Cross-plots of $\delta^{138}Ba$ versus Mn content, Sr content, and Mn/Sr ratios show no significant correlations (PR section: $r = 0.04$ for $\delta^{138}Ba$-Mn, $r = 0.30$ for $\delta^{138}Ba$-Sr, and $r = 0.02$ for $\delta^{138}Ba$-Mn/Sr; SP section: $r = 0.01$ for $\delta^{138}Ba$-Mn, $r = 0.15$ for $\delta^{138}Ba$-Sr, and

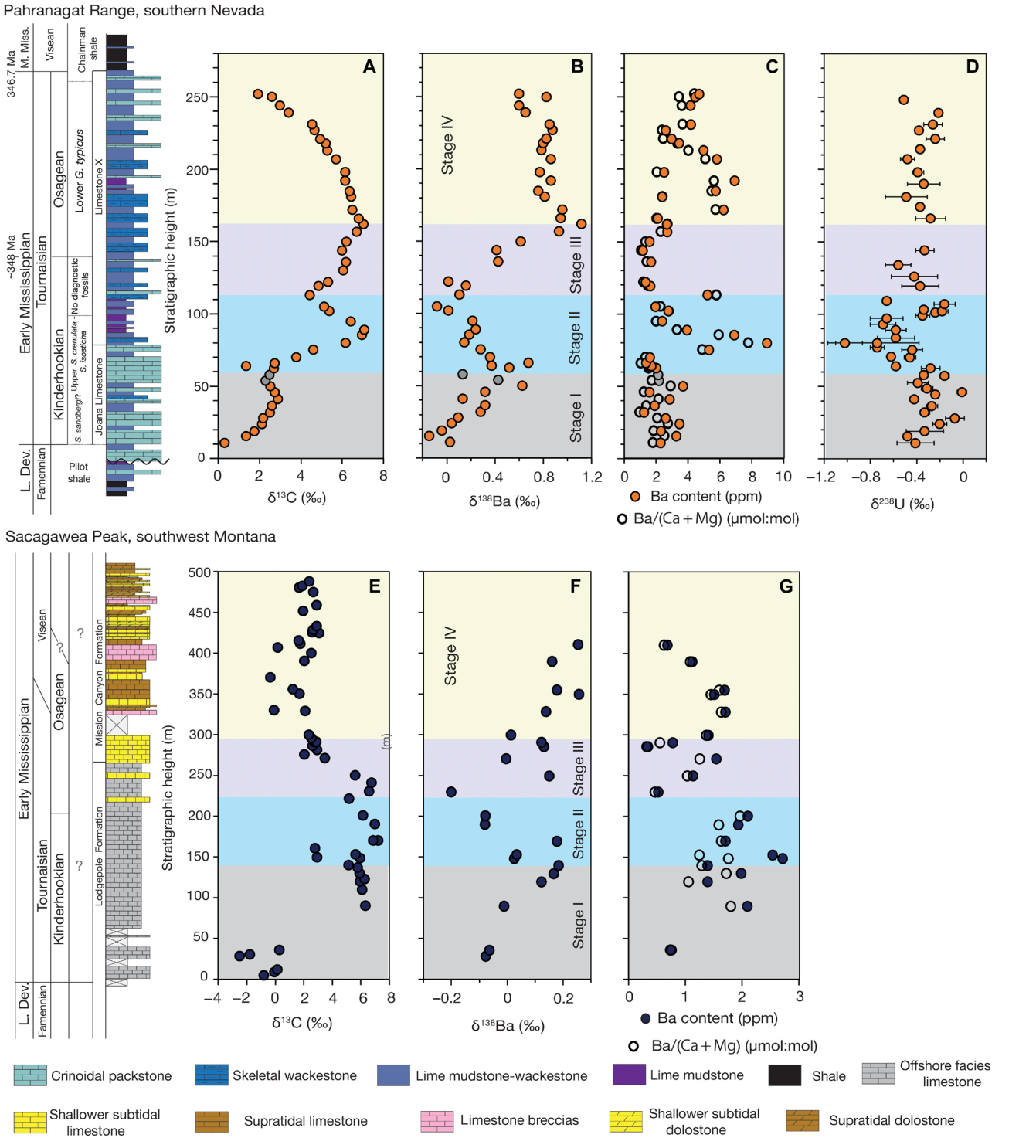

Fig. 2. The results for $\delta^{13}C_{carb}$, $\delta^{138}Ba$, $\delta^{238}U$, and [Ba] for the PR and SP sections. $\delta^{238}U$ data are from Cheng *et al.* (*8*). The geochemical profiles of $\delta^{13}C_{carb}$ (**A**), $\delta^{138}Ba$ (**B**), Ba content (**C**), $\delta^{238}U$ (**D**) for the PR section, and $\delta^{13}C_{carb}$ (**E**), $\delta^{138}Ba$ (**F**), Ba content (**G**) for the SP section. For each study site (PR and SP), all isotope data were generated from the same suite of samples. The two gray markers for the PR section represent samples with low $\delta^{18}O$ values (−8.56 and −8.40‰). L. Dev., Late Devonian; M. Miss., mid-Mississippian. *S. crenulata*, *Siphonodella crenulata*; *G. typicus*, *Gnathus typicus*; *S. sandbergi*, *Siphonodella sandbergi*; *S. isosticha*, *Siphonodella isosticha*.

$r = 0.31$ for δ^{138}Ba-Mn/Sr). These geochemical analyses, along with the geological evidence indicating the absence of subaerial diagenesis or exposure leading to meteoric alteration (*44*), suggest that burial diagenesis had a minimal influence on our study samples.

The effect of changes in mineralogy—such as the transformation of aragonite to calcite or dolomitization—on δ^{138}Ba is also likely to be small to negligible. Except for one sample from the SP section, which has a Mg/Ca value of 0.13, all samples have Mg/Ca values below 0.05, indicating that they have not been dolomitized. Measurements from modern carbonate precipitates demonstrate an isotopic offset of ~0.21‰ between seawater and aragonite, as well as a fractionation of ~0.13‰ between high-magnesium calcite and ambient seawater (*35*). Our study samples are primarily composed of calcite, while the original mineralogy of the samples is difficult to determine. However, given that our observed δ^{138}Ba excursions (from −0.15 to 1.12‰) are significantly larger than the isotopic fractionations associated with different carbonate mineralogies, changes in the original carbonate mineralogy likely had a negligible influence on our δ^{138}Ba records.

We examined the potential influence of local redox processes on δ^{138}Ba values by evaluating δ^{138}Ba against various redox-sensitive elements including Fe, V, Cr, and U concentrations (figs. S6 and S7). Cross-plots of δ^{138}Ba against these elements show no significant covariations (PR section: $r = 0.38$ for δ^{138}Ba-Fe, $r = 0.23$ for δ^{138}Ba-V, $r = 0.17$ for δ^{138}Ba-Cr, and $r = 0.22$ for δ^{138}Ba-U; SP section: $r = 0.02$ for δ^{138}Ba-Fe, $r = 0.04$ for δ^{138}Ba-V, $r = 0.19$ for δ^{138}Ba-Cr, and $r = 0.16$ for δ^{138}Ba-U). Last, we investigated the influence of local water depths on δ^{138}Ba records from our samples. We identified four main depositional facies within the studied section, as shown in Fig. 2. Overall, δ^{138}Ba distributions across these lithologic facies show no systematic differences (fig. S8), and δ^{138}Ba values change smoothly across facies transitions for the PR section (Fig. 2). Specifically, δ^{138}Ba values from packstone-grainstone (shallowest water) and lime mudstone (deepest water) show no statistical differences. We note that in the modern open ocean, barium isotopic gradients extend over a much larger distance, spanning several thousand kilometers, compared to the depths at which carbonate precipitation occurs in these study units (*24*). Therefore, the facies distribution observed in this study is not particularly unexpected.

In sum, results from these combined geochemical tracer and facies investigations suggest that δ^{138}Ba trends reflect secular variations of seawater δ^{138}Ba values in the Antler foreland basin. We further note that our measured δ^{138}Ba values are very heavy, and if our study samples were influenced by sediment buffering and deviated from the seawater values, then this would only indicate even higher local seawater δ^{138}Ba values. Therefore, our interpretation below is conservative.

Interpreting temporal barium isotope changes

The observed positive shift in δ^{138}Ba during stage I can be interpreted as an increase in the marine biological pump within the Antler foreland basin, which may increase the particulate organic carbon (POC) export flux and therefore pump surface Ba to intermediate water depths. In this process, the oxidative remineralization of sinking organic matter releases Ba, which reacts with sulfate to precipitate pelagic barite crystals, possibly in ephemeral, particle-associated microenvironments created by the oxidation of organic matter (*45*). Given that the Ba isotopic fractionation during barite precipitation from seawater is between −0.5 and −0.4‰, with the light isotope preferentially sequestered into barite (*27*, *29*, *30*), an enhanced biological pump leads to a shift of shallow-water δ^{138}Ba toward higher values and carbonates precipitating from seawater, reflecting those values albeit with a small offset (*26*, *29*, *46*, *47*). The gradual increase in δ^{138}Ba values during stage I thus reflects a shift toward a more productive surface marine system in the Antler foreland basin. An increase in the marine biological pump in stage I, thus enhancing organic carbon export and burial fluxes, is consistent with the observed shift toward more positive δ^{13}C values. An enhanced marine biological pump, in return, would have depleted water-column O_2 through oxidative remineralization, resulting in the expansion of marine anoxia. The onset of productivity-driven oceanic anoxia is supported by decreasing δ^{238}U values from late stage I to stage II, indicating an increase in the areal extent of anoxic/euxinic seafloor (Fig. 2). This scenario necessitates an increase in marine productivity well before the onset of anoxia, consistent with our paired Ba and U isotope records, where the δ^{138}Ba shift predates the δ^{238}U excursion. The trigger for an increase in the marine biological pump during the Tournaisian has been hypothesized to be linked to enhanced continental basalt weathering, which is evidenced by decreases in seawater $^{87}Sr/^{86}Sr$ ratios throughout the Tournaisian (*16*). However, a lack of sufficiently high-resolution age controls on the Sr isotope curve does not permit explicit links to continental weathering increases in stage I Ba isotope data. It has also been hypothesized that the rise and expansion of seed plants during the Tournaisian intensified chemical and physical weathering of silicate rocks, which delivered nutrients to the oceans and stimulated marine primary productivity and organic matter production (*14*, *16*). This hypothesis suffers from the fact that seed plant expansion spanned the entire Tournaisian rather than just stage I of this study, although pulses of land-plant expansion have previously been invoked to explain TICE-like events characterized by positive carbon excursions and global climate cooling (*48*). The net impact of land-plant expansion on continental weathering during the Devonian also remains poorly constrained (*49*). Thus, the potential cause-and-effect relationship between continental weathering and the marine biological pump in the early Tournaisian ocean remains a question that merits future investigation.

The negative δ^{138}Ba shift during stage II is interpreted as the result of pelagic barite dissolution and Ba release under anoxic/euxinic conditions facilitated by microbial sulfate reduction. Expanded anoxia/euxinia at this time is supported by a widespread negative δ^{238}U shift, and previous mass balance modeling suggests a ~17-fold increase in anoxic/euxinic seafloor area (covering <2 to ~35% of seafloor area) (*8*). Under anoxic/euxinic conditions, barite dissolution would release isotopically light Ba from the sediments to the water column, leading to high [Ba] and low δ^{138}Ba values in the water column (*20*, *24*, *29*). The δ^{138}Ba and [Ba] trends from stage II (and the subsequent stage III) display a moderate negative correlation where lower δ^{138}Ba values correspond to higher [Ba] (fig. S9), further supporting the interpretation that Ba was inherited from the regional dissolution of pelagic barite. Given that many of the δ^{138}Ba values in stage II drop to levels significantly below modern riverine input values of ~0.2‰ (*24*), we suggest three scenarios that may be compatible with our observations. These three scenarios include the upwelling of anoxic deep waters into shallow-water environments (scenario no. 1, which refers to the vertical movement of deep, nutrient-rich waters to the surface and can lead to localized anoxia in shallow environments), the expansion of shallow-water anoxia (i.e., anoxia developed above 100m water depth) (scenario no. 2) (*50*), or strengthening of ocean overturning circulation (scenario no. 3, which refers to the increased movement of water masses in the

ocean's circulation patterns and has broader implications for the distribution of marine nutrients over extensive geographic distances) in the Antler foreland basin. All three scenarios could return isotopically light Ba from deeper waters to the surface. However, upwelling processes (scenario no. 1) are typically associated with a transient negative $\delta^{13}C$ excursion because deeper anoxic waters have lower $\delta^{13}C$ values owing to organic matter degradation at depth. This scenario appears to be inconsistent with the $\delta^{13}C$ record during stage II where $\delta^{13}C$ values increase rather than decrease. The low $\delta^{138}Ba$ values are consistent with extensive shallow-water anoxia/euxinia (scenario no. 2) that would shift the location of barite reduction from deeper-water to shallower-water environments. Our inference of shallow-water anoxia/euxinia is consistent with a prior study that used sediment-derived redox interpretations to identify local anoxia in the Antler foreland basin (*8*). Alternatively, strengthening oceanic circulation (i.e., faster water mass exchange between surface and deep waters) (scenario no. 3) is also consistent with Early Mississippian climatic cooling as inferred from conodont apatite oxygen isotopes (*16*) and carbonate $\delta^{15}N$ records (*15*). In this stage II scenario, recycled nutrients (e.g., phosphorus) from the anoxic bottom waters of the Antler foreland basin enhanced ocean anoxia and provided nutrients for primary productivity, thereby facilitating organic carbon export through the water column (*4*). Therefore, the negative $\delta^{138}Ba$ excursion and low $\delta^{138}Ba$ values during stage II do not necessarily indicate low-productivity oceans; instead, they signify a high-productivity surface marine system, as is also supported by various other evidence from the TICE interval, such as $\delta^{15}N$ and $\delta^{66}Zn$ data (*15*, *17*).

We interpret the gradual increase in $\delta^{138}Ba$ values during stage III as the result of a reduction in the extent of seafloor anoxia/euxinia, which we infer from increasing $\delta^{238}U$ values from late stage II to early stage III and the consistently high $\delta^{238}U$ values recorded during stage III (*8*). We suggest that a decrease in the areal extent of seafloor anoxia reduced barite dissolution via microbial sulfate reduction, while at the same time, pelagic barite precipitation was able to resume. This led to a gradual recovery toward a modern ocean–like pattern of barium isotope distributions and an increase in surface seawater $\delta^{138}Ba$ values. During stage IV, $\delta^{138}Ba$ values remained relatively stable at high values, significantly higher than the UCC or riverine inputs (*38*, *51*). These high $\delta^{138}Ba$ values suggest persistently high marine export production under more oxic marine conditions. The decreasing $\delta^{13}C$ values at this time suggest that the more oxic conditions led to a reduction in organic carbon burial flux (i.e., possibly due to intense oxidative organic matter remineralization).

The similarities in stratigraphic trends together with the observed differences in absolute isotopic values between the two widely separated sections suggest a likely global control on $\delta^{138}Ba$ trends, with local variations superimposed upon it. We propose that the fact that nearly identical stratigraphic $\delta^{138}Ba$ trends are observed in our two widely separated sections, but with very different absolute $\delta^{138}Ba$ values (Fig. 2), can be reconciled when considering that the Ba isotope proxy is inherently regional. The muted $\delta^{138}Ba$ changes at SP may reflect changes in the marine biological pump weaker than at PR and/or different redox conditions that modulated the capacity of each study site to record changes in export productivity. Hereafter, we assess the robustness of our proposed series of events by means of Earth system modeling and show that our simulations support the second explanation implying a modulation of $\delta^{138}Ba$ signals by local redox conditions.

A physically consistent series of events confirmed by Earth system modeling

We conducted a gridded ensemble of simulations using the Earth system model of intermediate complexity cGENIE (*36*, *52*), configured with Early Mississippian boundary conditions (Materials and Methods), to investigate the relationships between global climate, marine productivity, and oceanic oxygenation during the TICE. We adopted a continental reconstruction for the Early Mississippian (fig. S10), adjusted the model solar luminosity (*53*), and set the atmospheric O_2 concentration (pO_2) to its present-day value (*54*). Phosphate was defined as the single limiting nutrient. The two axes of our gridded ensemble of simulations were the atmospheric pCO_2 that we varied between ×1 and ×8 preindustrial (280 ppm) concentrations (*54*) and the mean ocean phosphate concentration ($[PO_4]$) that we varied from ×0.2 to ×2.0 of the present-day mean oceanic concentration of 2.159 μmol kg^{-1}. All simulations were run for 25,000 model years.

We looked for the best plausible scenario to explain available proxy data during the TICE. A first constraint was provided by published conodont apatite oxygen isotope ($\delta^{18}O_{apatite}$) data that indicated a drop in sea surface temperature (SST) from ~31° to ~26°C across the TICE (fig. S11) (*2*, *16*). This cooling was best captured in the model by a decrease in pCO_2 from ×8 to ×2 preindustrial CO_2 levels (fig. S12). With these constraints in mind, we identified a trajectory in the pCO_2 – $[PO_4]$ space, which captured the changes in $\delta^{138}Ba$ and $\delta^{238}U$ during the TICE (Fig. 3). The geochemical landscape for stage I (see Fig. 2) would match our simulation conducted for ×8 CO_2 and ×1.2 $[PO_4]$. Under these conditions, the global extent of seafloor anoxia approximates the modern value (label no. 1 in Fig. 3A), which is in agreement with $\delta^{238}U$ (Fig. 2). At the same time, POC export production amounts to 1.4 mol m^{-2} $year^{-1}$ at the PR (Fig. 3C), and the ocean is locally well oxygenated in this area (label no. 1 in Fig. 4A). Stage II is reproduced by decreasing pCO_2 from ×8 to ×4 preindustrial CO_2 levels (as a first step in cooling) and increasing $[PO_4]$ from ×1.2 to ×1.6 $[PO_4]$ (or equivalently, +33%). The areal extent of benthic anoxia rises to 32% of the global seafloor area, and export productivity increases by nearly 60% at the PR (label no. 2 in Fig. 3, A and C). According to our interpretation of the proxy database for stage II, anoxia is expected to develop at PR, which would explain the $\delta^{138}Ba$ decrease taking place in a background of rising $\delta^{13}C_{carb}$. Only accounting for changes in pCO_2 and $[PO_4]$ does not permit simulating any large decrease in subsurface oceanic dissolved oxygen concentrations $[O_2]$ at the PR (dashed arrow in Fig. 4A). This model-data mismatch can be resolved by accounting for regional sea level change. As testified by the changes in lithology from grainstones/packstones to wackestones/mudstones (Fig. 2), it appears that sea level significantly rose at PR during stage II (fig. S13). Accounting for this temporary deepening of the section permits the ability to capture the expansion of anoxia at the PR during stage II (solid red path in Fig. 4, A and B). Last, stages III and IV are simulated by maintaining $[PO_4]$ at ×1.6 and further decreasing pCO_2 from ×4 to ×2 CO_2. Global cooling induces a further increase in export production at PR by 14% (from 2.2 to 2.5 mol m^{-2} $year^{-1}$; label no. 3 in Fig. 3C). The concomitant sea level fall (fig. S13) allows ocean $[O_2]$ to increase back to predeepening values at PR (label no. 3 in Fig. 4, A and B). We note, however, that the simulated global extent of seafloor anoxia, although it decreases, does not reach modern-like levels (Fig. 3A) in disagreement with $\delta^{238}U$ data (Fig. 2). Additional simulations show that solving this model-data discrepancy requires invoking a rise in atmospheric pO_2. A pO_2 increase of 25%

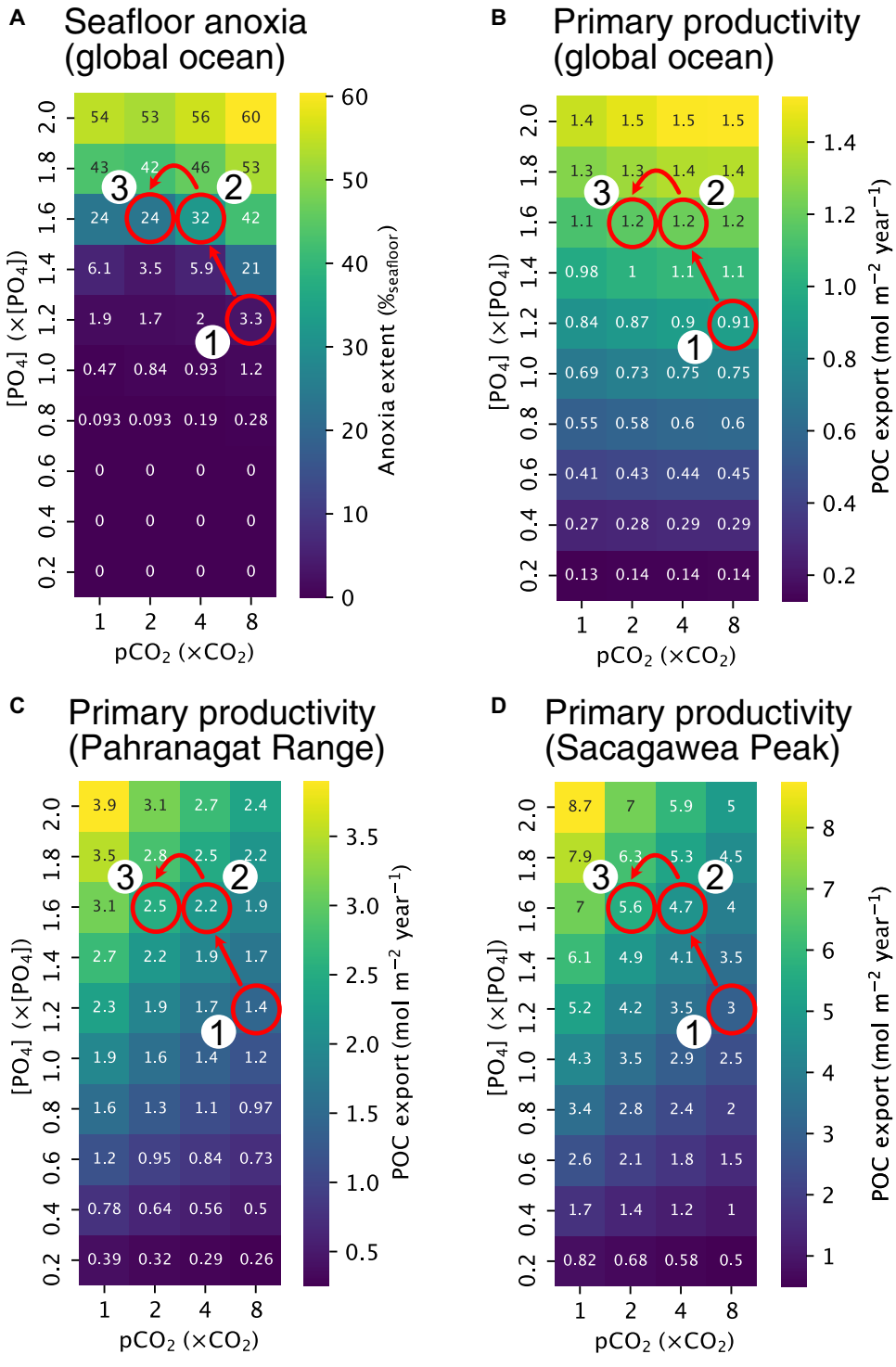

Fig. 3. Seafloor anoxia and primary productivity in the Earth system model cGENIE. (**A**) The extent of seafloor anoxia as a function of pCO_2 and PO_4 inventory. Each cell represents a single simulation. Numbers and colors represent the extent of anoxia (defined as the percentage of the global benthic surface characterized by seafloor $[O_2] \leq 0$ µmol kg^{-1}). Red arrows and labels represent our preferred scenario discussed in the text, selected to capture the changes in ocean temperatures, benthic anoxia, and primary productivity. (**B**) As per (A) for the POC export production simulated globally. (**C**) As per (B) for POC export at PR. (C) As per (B) for SP. Note the different color scales used in each panel.

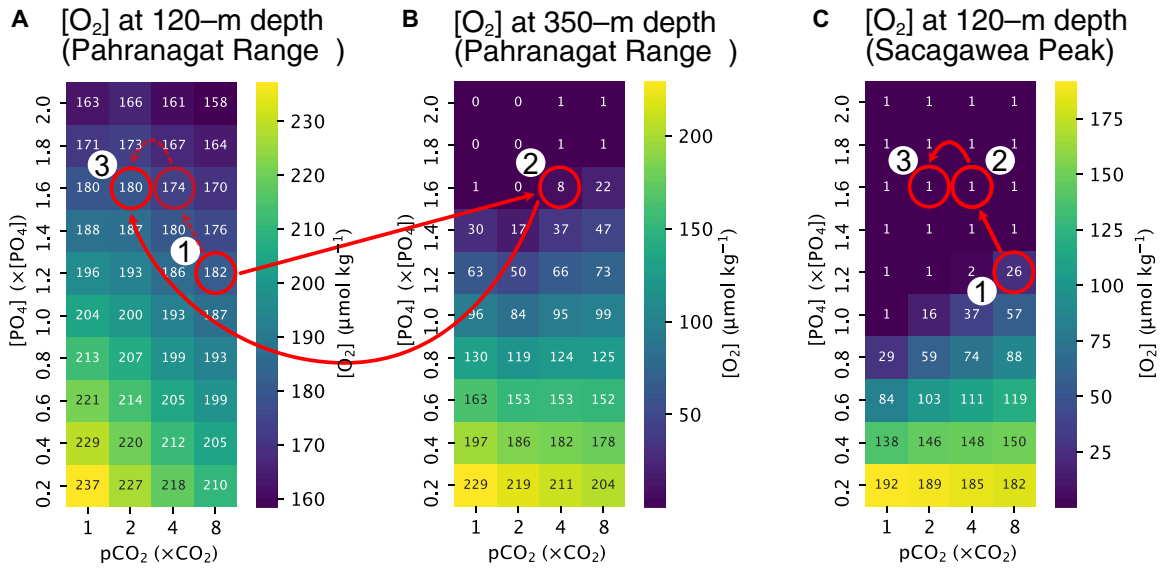

Fig. 4. Ocean [O_2] in the Earth system model cGENIE. (**A** and **B**) Ocean [O_2] at PR as a function of pCO_2 and PO_4 inventory at 120 m (A) and 350 m (B) below sea level. Red arrows and labels represent scenarios discussed in the text. (**C**) Ocean [O_2] at SP as a function of pCO_2 and PO_4 inventory at 120 m below sea level. Sea level changes happening at SP are expected to be the same as at PR but could not be represented here because the bathymetry at SP is too shallow in our paleogeographical reconstruction for 360 Ma interpolated at the cGENIE model resolution. However, we note that sea level rise would, if anything, further lower ocean [O_2]; the simulation of the extent of anoxia at SP is therefore not affected by this bathymetric feature, and anoxia at SP stands out as a robust model result that is poorly dependent on the model bathymetry. Note the different color scales used in each panel.

(from ×1 to ×1.25 modern) is sufficient to reconcile our simulations with uranium isotope proxy data (fig. S14). This increase in atmospheric pO_2 may have resulted from the burial of organic carbon (*55*), such as reflected by the large $\delta^{13}C$ excursion, which constitutes a net source of atmospheric oxygen at the million-year timescale. An atmospheric pO_2 increase was similarly documented during the late Cambrian Steptoean positive carbon isotope excursion (*56*). Because of the large uncertainties in boundary conditions and model simplifications, our Earth system model simulations are not aimed at providing an accurate reconstruction of Earth system conditions during the TICE. In particular, changes in atmospheric pCO_2 invoked to explain SST proxy data are dependent on the model's climatic sensitivity. Similarly, the response of export production and ocean oxygenation to nutrient loading is expected to be model dependent, and other specific values of changes in ocean nutrient concentrations may be necessary to simulate similar environmental changes using models of higher complexity and/or higher spatial resolution. However, and keeping these limitations in mind, our numerical simulations permit demonstrating that the series of events proposed to explain proxy records during the TICE is plausible in a physically consistent Earth system model.

Our simulations also allow us to propose an explanation for the muted changes in $\delta^{138}Ba$ at SP. This second section was located closer to the coast and slightly north of the PR section during the TICE, thus closer to the core of the west Laurentian upwelling system and oxygen minimum zone (fig. S10). In the model, absolute values of export production are two times higher at the SP section than at the PR section, and they undergo similar relative changes during the TICE (+57 and then +14% at PR compared to +57 and +19% at SP; Fig. 3, C and D). Simulated changes in export production thus provide no explanation for the muted changes in $\delta^{138}Ba$ at SP. The direct consequence of higher primary productivity at SP, however, is a higher consumption of ocean oxygen during the remineralization of sinking organic matter, which locally depletes ocean water in dissolved O_2 (compare Fig. 4, A and C). Locally anoxic conditions may induce the dissolution of sinking pelagic barite, and the resulting negative shift in $\delta^{138}Ba$ would mask the positive shift associated with the high productivity levels (fig. S1). Our model results suggest that the local development of anoxic conditions would have limited the recording of productivity signals in the TICE $\delta^{138}Ba$ record of SP.

This assimilation of geochemical data in an Earth system model permits better constraining of the mechanisms that led to middle Tournaisian oceanic anoxia. The latter contrasts with Permian-Triassic oceanic anoxia (*57*) and many other oceanic anoxic events during the Mesozoic (*58*), which were linked to the warming-induced expansion of anoxia. Similar to the end-Hirnantian (Late Ordovician) oceanic anoxic event (*52*), middle Tournaisian ocean anoxia occurred in the context of global climate cooling (fig. S11). Our simulations suggest that, contrary to the end-Hirnantian, however, the Tournaisian oceanic anoxia required not only global cooling (and associated changes in deep-ocean circulation) but also a rise in ocean nutrient concentrations (Fig. 3). This is because, unlike the Ordovician, no major reorganization of ocean circulation takes place in our cGENIE simulations for the Tournaisian, at least within the range of pCO_2 values selected to match proxy-derived SSTs. Assimilation of the proxy database in our Earth system model demonstrates an increase in global export productivity by around 30%, resulting from an increase in ocean nutrient inventories of the same order of magnitude (from ×1.2 to ×1.6 [PO_4]; Fig. 3B), is required to explain the concomitant changes in SSTs, global extent of anoxia, regional oceanic [O_2] changes, and regional changes in primary productivity documented in the Antler basin based on $\delta^{138}Ba$. Although underlying mechanisms are still to be defined, an increase in continental weathering linked to the spread of land plants (*49*), or enhanced continental basalt weathering (*16*), may constitute likely triggers for the increase in oceanic nutrient concentrations and the spread of anoxic conditions.

Implications for the Early Mississippian Earth-life system

Our barium concentration and isotope results, combined with numerical simulations, provide critical evidence supporting the hypothesis that an enhanced marine biological pump had an important role in driving the TICE event in the Antler foreland basin. Inferences from increased productivity in our study areas support links between the enhanced burial of organic matter during the TICE interval and the drawdown of atmospheric pCO_2, which likely contributed to the Early Mississippian (Tournaisian) cooling and the initiation of the LPIA (*2*, *59*). Tournaisian seawater cooling of ~5°C at equatorial latitudes is indicated by oxygen isotope records of conodont apatite (fig. S11) (*2*, *16*) and is supported by the occurrence of glacial sedimentary deposits in both low and high latitudes (*60*, *61*).

High-resolution reconstructions of marine biodiversity throughout the Paleozoic indicate that biodiversity plateaued during the early Silurian and peaked in the early Middle Devonian, followed by a significant decline and sustained low levels after the Late Devonian (Frasnian/Famennian) mass extinction event (*9*). Biotic diversity did not recover until after the mid-Mississippian (middle Visean), indicating a ~20-Myr delay in recovery (*9*, *10*). Notably, the recovery period following the Late Devonian extinction was even more prolonged than the recovery after the end-Permian mass extinction, which is often attributed to repeated environmental disturbances such as oceanic anoxia and high SSTs (*57*, *62*). Our barium isotope results suggest productivity-driven perturbations to the carbon cycle at least within the Antler foreland basin. Our Earth system model experiments further demonstrate that the increase in productivity in the Antler foreland basin may have reflected a global perturbation, with global export productivity increasing by around +30% in our simulations. Results from our coupled model-data approach, along with previous studies on seawater redox and stable isotopes (*5*, *8*, *15*, *16*), suggest that dynamic oceanic conditions—particularly with respect to increases in the marine biological pump and expanded anoxia in the Early Mississippian oceans—may have contributed to the slow recovery of biodiversity in the late Paleozoic.

Summary

We generated high-resolution [Ba] and $\delta^{138}Ba$ curves through well-dated limestones across the Early Mississippian (Tournaisian) carbon isotope excursion in western Laurentia. The range of stratigraphic and geochemical data suggests that the $\delta^{138}Ba$ trends represent a primary oceanographic signal of the Antler foreland basin rather than variations related to diagenesis or regional depositional processes. We interpret the following sequence of events spanning the ~4-Myr-long TICE: Increasing $\delta^{138}Ba$ trends (stage I) are interpreted to be a result of increased marine export productivity likely caused by enhanced continental weathering, leading to enhanced organic carbon burial and increased $\delta^{13}C_{carb}$. Decreasing $\delta^{138}Ba$ values (stage II) associated with a negative $\delta^{238}U$ shift are interpreted to represent the expansion of seafloor anoxia/euxinia, which promoted barite dissolution in shallower-water settings. The gradual recovery of $\delta^{138}Ba$ values and rising $\delta^{13}C_{carb}$ isotopic values during stages III and the subsequent stabilization of $\delta^{138}Ba$ during the recovery stage of the TICE (stage IV) suggest a return to less anoxic conditions. This series of events is qualitatively supported by a physically consistent Earth system model representing the coupled changes in climate and marine biogeochemistry in a spatially resolved, three-dimensional (3D) ocean. In these simulations, marine export productivity increases by around +30% during the TICE. Together, our $\delta^{138}Ba$ data and Earth system model simulations suggest that high marine export productivity was responsible for enhanced organic carbon burial and oceanic anoxia, leading to Early Mississippian cooling and the initiation of the LPIA. Therefore, the highly dynamic oceanic conditions during the Early Mississippian may help to explain the documented low biodiversity during the Tournaisian.

MATERIALS AND METHODS

Geological background

During the Early Carboniferous, North America (Laurentia) straddled the paleoequator, and convergence along its western margin led to the development of the Antler foreland basin, which extended from north Nevada to Canada (Fig. 1). During the Early Carboniferous, the PR study area accumulated carbonate-dominated distal foreland deposits, representing shallow through deeper marine environments (*6*). The SP succession represents slope, deep ramp through shallow ramp deposits accumulating along the distal foreland basin (*44*). The two study sections are separated by ~1300 km.

For the current study, we sampled the Lower Mississippian Joana Limestone and Limestone X from the PR section and the Lower Mississippian Lodgepole Formation and Mission Canyon Formation from the SP section (Fig. 2). The stratigraphy at the PR location has been described in detail by Saltzman *et al.* (*7*) and Maharjan *et al.* (*6*). Briefly, the 86-m-thick Joana Limestone is dominated by crinoid-rich grainstone and packstone (representing upper shoreface environments), and the overlying 186-m-thick Limestone X consists mainly of lime mudstone and wackestone, with subordinate thin packstone and grainstone storm interbeds (representing offshore to lower shoreface environments). The stratigraphy at the SP location has been described in detail by Katz *et al.* (*63*) and Buoniconti (*64*). Briefly, the ~250-m Lodgepole Formation consists of deeper subtidal (offshore/slope) limestone, and the overlying >300-m-thick Mission Canyon Formation consists mainly of shallow subtidal limestone, solution-collapse limestone breccias, and shallow subtidal dolostone (*44*, *63*, *64*). The carbon isotope stratigraphy and conodont biostratigraphy of the PR and SP sections were previously investigated by Saltzman *et al.* (*7*, *59*), Buoniconti (*64*), Katz *et al.* (*63*), Maharjan *et al.* (*6*), and Cheng *et al.* (*8*), providing a high-resolution temporal framework for the study sections. Forty-seven limestone samples from the PR section and 30 samples from the SP section were analyzed for $\delta^{138}Ba$ and major and trace elements in this study.

Using barium isotope in marine carbonates to track paleoproductivity change

The Ba isotope composition of marine carbonates is emerging as a promising proxy to track marine export production in the oceans (*18*, *19*). The major source of Ba to the ocean is riverine inputs primarily via continental weathering with an average $\delta^{138}Ba_{river}$ of ~0.2‰ (*24*). The average UCC has a high Ba content of ~600 μg/g (*37*) and a $\delta^{138}Ba_{UCC}$ of 0.00 ± 0.04‰ (*38*). Pelagic precipitation (precipitation of discrete, micrometer-sized crystals in the seawater column) of barite in the modern ocean constitutes the major seawater sink for Ba (*65*).

The vertical distribution of $[Ba]_{diss}$ and its isotopes in seawater depends on the precipitation of pelagic barite through microbial remineralization of sinking organic matter and the partial dissolution of barite particles at depth associated with microbial sulfate reduction (fig. S1) (*24*, *28*). Barite precipitation from seawater is associated with a large and detectable isotopic fractionation with barite crystals enriched

in the light isotope ($\delta^{138}Ba_{barite\text{-}diss} = \delta^{138}Ba_{barite} - \delta^{138}Ba_{diss} \approx -0.5‰ - -0.4‰$, where $\delta^{138}Ba_{diss}$ denotes the isotopic composition of $[Ba]_{diss}$ in seawater) (*27*, *29*, *30*). In contrast, barite dissolution is associated with very limited isotopic fractionation, similar to that of laboratory analytical uncertainty (*18*, *24*, *27*, *30*). Therefore, during periods of increased marine export productivity, the enhanced carbon export flux would pump more Ba from the surface to deep waters, decreasing the $[Ba]_{diss}$ in surface waters and shifting the $\delta^{138}Ba_{diss}$ of those regional waters to higher values. In contrast, when waters become more anoxic at depth, the dissolution of sinking pelagic barite returns the isotopically light Ba isotopes to seawater and leads to regional increases in seawater $[Ba]_{diss}$ and negative shifts in $\delta^{138}Ba_{diss}$ (*24*, *29*). In the modern Pacific Ocean, the deep water (i.e., >1500 m) typically has high $[Ba]_{diss}$ (~150 nmol kg^{-1}) and low $\delta^{138}Ba_{diss}$ values (~0.2‰), while Pacific surface waters have low $[Ba]_{diss}$ (~35 nmol kg^{-1}) and high $\delta^{138}Ba_{diss}$ values (~0.6‰) (*34*). The residence time of Ba in modern seawater is partly on the order of the scale of ocean mixing in the modern ocean (*24*), implying that the Ba isotope proxy is a regional rather than a global paleoceanographic proxy and potentially displaying sensitivity to ocean circulation changes (*24*). The $\delta^{138}Ba$ values of carbonate sediments have been attempted to reconstruct changes in the marine biological pump in Ediacaran, Late Silurian, and Paleocene-Eocene oceans (*18*–*20*).

Analytical methods

The fragments of rock chips were cleaned using deionized water and dried with compressed air, and fresh fragments without veins were chosen and powdered to ~200 mesh. The powders were dissolved using a well-developed sequential extraction procedure to effectively extract the Ba fraction in lattices of carbonate minerals [see details in Lin *et al.* (*35*) and Zhang *et al.* (*20*)]. After treating with Milli-Q water and 1 M ammonium acetate buffer solution to remove any Ba from the water-soluble fraction and exchangeable phases, the samples were dissolved in 1 M acetic acid to extract Ba from carbonate minerals. The resultant solution was dried down on a hot plate at 100°C. After complete dry-down, the samples were dissolved and stored in 6 M HCl for elemental and isotopic analysis. An aliquot of each stock solution was dried down and redissolved in 3% HNO_3 for major and trace element analyses. The major and trace elements were measured with a Thermo Element XR HR-ICP-MS at the Center for Research and Education on Biological Evolution and Environment (CREBEE), Nanjing University, with analytical errors better than 5%. An aliquot of solution corresponding to 200 ng of Ba was taken out from the stock solution and mixed with ^{130}Ba-^{135}Ba double spikes at a sample:spike ratio of 4:1. Then, the mixtures were dried down for complete equilibrium and redissolved in 2.5 M HCl for ion-exchange column separation (*20*, *35*). Ba isotope ratios were measured on a Thermo Neptune XT MC-ICP-MS at the CREBEE, Nanjing University. The standard solution National Institute of Standards and Technology SRM3104a (100-ppb Ba) and a barite standard GSO-2 were analyzed after every five samples. The Ba isotopic compositions ($\delta^{138}Ba$) of standards SRM3104a and GSO-2 are 0.00 ± 0.045 ‰ [two standard deviations (SD), $n = 14$] and 0.29 ± 0.035‰ (two SD, $n = 9$), respectively.

Earth system model simulations

Description of the model

cGENIE is an Earth system model of intermediate complexity offering a coupled representation of climate and marine biogeochemistry in a 3D ocean (*36*). The model climatic component consists of a 3D frictional geostrophic ocean circulation model coupled with a 2D energy-moisture-balance atmospheric model and a sea ice model. We ran cGENIE on a 36 by 36 equal-area grid with 17 ocean vertical levels extending down to ~5900-m depth. The cycling of carbon and associated tracers in the ocean is based on a single (phosphate) nutrient limitation of biological productivity following Pohl *et al.* (*52*). Compared with recent climate models of the Coupled Model Intercomparison Project phase 6, the simplified representation of climate in cGENIE offers a rapid model integration time, facilitating the numerous sensitivity tests necessary to assess the impact of the large uncertainties in boundary conditions in the deep geological past, as well as the >10,000-year-long model experiments required to ensure deep-ocean equilibrium. Despite its lower spatial resolution, cGENIE satisfactorily simulates first-order spatial patterns and values of ocean circulation and biogeochemistry in the modern (*36*, *66*) and geological past (*52*, *67*, *68*).

Description of the numerical experiments

We configured cGENIE with Early Tournaisian boundary conditions using the 360-Ma model configuration of Pohl *et al.* (*68*). Specifically, we used the 360-Ma paleogeography of Scotese and Wright (*69*) (fig. S10), lowered the solar luminosity value to 1327 W m^{-2} (*53*), and used a null eccentricity-minimum obliquity orbital configuration, which provides an equal mean annual insolation to both hemispheres with minimum seasonal contrasts. We fixed the atmospheric oxygen concentration to the present-day value of 20.95% in agreement with results obtained with long-term carbon cycle models (*54*).

Simulations were initialized with a sea ice–free ocean and homogeneous temperature and salinity in the ocean (5°C and 33.9‰, respectively). The model was then integrated for 25,000 years, saving the results every 100 years over the past 5000 years. Results averaged over the past 5000 years were used for this analysis to account for the potential impact of oscillations in the deep ocean circulation and resulting temporal variations in ocean quantities (*68*).

Supplementary Materials

The PDF file includes:

Figs. S1 to S14
Legends for tables S1 and S2
References

Other Supplementary Material for this manuscript includes the following:

Tables S1 and S2

REFERENCES AND NOTES

1. H.-s. Mii, E. L. Grossman, T. E. Yancey, Carboniferous isotope stratigraphies of North America: Implications for Carboniferous paleoceanography and Mississippian glaciation. *Geol. Soc. Am. Bull.* **111**, 960–973 (1999).
2. W. Buggisch, M. M. Joachimski, G. Sevastopulo, J. R. Morrow, Mississippian $\delta^{13}C_{carb}$ and conodont apatite $\delta^{18}O$ records—Their relation to the Late Palaeozoic glaciation. *Palaeogeogr. Palaeoclimatol. Palaeoecol.* **268**, 273–292 (2008).
3. I. P. Montañez, C. J. Poulsen, The late Paleozoic ice age: An evolving paradigm. *Annu. Rev. Earth Planet. Sci.* **41**, 629–656 (2013).
4. M. R. Saltzman, E. Groessens, A. V. Zhuravlev, Carbon cycle models based on extreme changes in $\delta^{13}C$: An example from the lower Mississippian. *Palaeogeogr. Palaeoclimatol. Palaeoecol.* **213**, 359–377 (2004).
5. L. Yao, W. Qie, G. Luo, J. Liu, T. J. Algeo, X. Bai, B. Yang, X. Wang, The TICE event: Perturbation of carbon–nitrogen cycles during the mid-Tournaisian (Early Carboniferous) greenhouse–icehouse transition. *Chem. Geol.* **401**, 1–14 (2015).
6. D. Maharjan, G. Jiang, Y. Peng, M. J. Nicholl, Sulfur isotope change across the early Mississippian K–O (Kinderhookian–Osagean) $\delta^{13}C$ excursion. *Earth Planet. Sci. Lett.* **494**, 202–215 (2018).
7. M. R. Saltzman, L. A. González, K. C. Lohmann, Earliest Carboniferous cooling step triggered by the Antler orogeny? *Geology* **28**, 347–350 (2000).

8. K. Y. Cheng, M. Elrick, S. J. Romaniello, Early Mississippian ocean anoxia triggered organic carbon burial and late Paleozoic cooling: Evidence from uranium isotopes recorded in marine limestone. *Geology* **48**, 363–367 (2020).
9. J.-X. Fan, S.-Z. Shen, D. H. Erwin, P. M. Sadler, N. M. Leod, Q.-M. Cheng, X.-D. Hou, J. Yang, X.-D. Wang, Y. Wang, H. Zhang, X. Chen, G.-X. Li, Y.-C. Zhang, Y.-K. Shi, D.-X. Yuan, Q. Chen, L.-N. Zhang, C. Li, Y.-Y. Zhao, A high-resolution summary of Cambrian to Early Triassic marine invertebrate biodiversity. *Science* **367**, 272–277 (2020).
10. L. Yao, M. Aretz, P. B. Wignall, J. Chen, D. Vachard, Y. Qi, S. Shen, X. Wang, The longest delay: Re-emergence of coral reef ecosystems after the Late Devonian extinctions. *Earth Sci. Rev.* **203**, 103060 (2020).
11. J. L. Isbell, L. C. Henry, E. L. Gulbranson, C. O. Limarino, M. L. Fraiser, Z. J. Koch, P. L. Ciccioli, A. A. Dineen, Glacial paradoxes during the late Paleozoic ice age: Evaluating the equilibrium line altitude as a control on glaciation. *Gondw. Res.* **22**, 1–19 (2012).
12. P. K. Swart, Global synchronous changes in the carbon isotopic composition of carbonate sediments unrelated to changes in the global carbon cycle. *Proc. Natl. Acad. Sci. U.S.A.* **105**, 13741–13745 (2008).
13. M. G. Braun, N. T. Anderson, K. D. Bergmann, E. M. Griffith, M. R. Saltzman, Early Mississippian global $\delta^{13}C$ excursion is not a diagenetic artifact. *Geology* **52**, 641–645 (2024).
14. T. J. Algeo, R. A. Berner, J. B. Maynard, S. E. Scheckler, Late Devonian oceanic anoxic events and biotic crises: "Rooted" in the evolution of vascular land plants. *GSA Today* **5**, 45 (1995).
15. J. Liu, T. J. Algeo, W. Qie, M. R. Saltzman, Intensified oceanic circulation during Early Carboniferous cooling events: Evidence from carbon and nitrogen isotopes. *Palaeogeogr. Palaeoclimatol. Palaeoecol.* **531**, 108962 (2019).
16. B. Chen, J. Chen, W. Qie, P. Huang, T. He, M. M. Joachimski, M. Regelous, P. A. E. Pogge von Strandmann, J. Liu, X. Wang, I. P. Montañez, T. J. Algeo, Was climatic cooling during the earliest Carboniferous driven by expansion of seed plants? *Earth Planet. Sci. Lett.* **565**, 116953 (2021).
17. Y. Zhong, J. Chen, S.-A. Liu, C. Yuan, B. Gao, T. T. Isson, T. J. Algeo, Q. Sheng, B. Chen, G. Luo, X.-d. Wang, W. Qie, Zinc isotope perspective on global carbon cycling during the onset of the late Paleozoic icehouse. *Geology* **53**, 99–104 (2025).
18. L. Bridgestock, Y.-T. Hsieh, D. Porcelli, G. M. Henderson, Increased export production during recovery from the Paleocene–Eocene thermal maximum constrained by sedimentary Ba isotopes. *Earth Planet. Sci. Lett.* **510**, 53–63 (2019).
19. W. Wei, Z. Zeng, J. Shen, L.-L. Tian, G.-Y. Wei, H.-F. Ling, F. Huang, Dramatic changes in the carbonate-hosted barium isotopic compositions in the Ediacaran Yangtze Platform. *Geochim. Cosmochim. Acta* **299**, 113–129 (2021).
20. F. Zhang, J. Frýda, M. Fakhraee, Y.-b. Lin, G.-Y. Wei, M. Cao, N. Li, J. Zhou, B. Frýdová, H. Wei, S.-z. Shen, Marine anoxia as a trigger for the largest Phanerozoic positive carbon isotope excursion: Evidence from carbonate barium isotope record. *Earth Planet. Sci. Lett.* **584**, 117421 (2022).
21. F. Dehairs, R. Chesselet, J. Jedwab, Discrete suspended particles of barite and the barium cycle in the open ocean. *Earth Planet. Sci. Lett.* **49**, 528–550 (1980).
22. M. Eagle, A. Paytan, K. R. Arrigo, G. van Dijken, R. W. Murray, A comparison between excess barium and barite as indicators of carbon export. *Paleoceanography* **18**, 1021 (2003).
23. A. Paytan, E. M. Griffith, Marine barite: Recorder of variations in ocean export productivity. *Deep-Sea Res. II Top. Stud. Oceanogr.* **54**, 687–705 (2007).
24. T. J. Horner, P. W. Crockford, *Barium Isotopes: Drivers, Dependencies, and Distributions Through Space and Time* (Cambridge Univ. Press, 2021).
25. J. K. B. Bishop, The barite-opal-organic carbon association in oceanic particulate matter. *Nature* **332**, 341–343 (1988).
26. T. J. Horner, C. W. Kinsley, S. G. Nielsen, Barium-isotopic fractionation in seawater mediated by barite cycling and oceanic circulation. *Earth Planet. Sci. Lett.* **430**, 511–522 (2015).
27. T. J. Horner, H. V. Pryer, S. G. Nielsen, P. W. Crockford, J. M. Gauglitz, B. A. Wing, R. D. Ricketts, Pelagic barite precipitation at micromolar ambient sulfate. *Nat. Commun.* **8**, 1342 (2017).
28. P. W. Crockford, B. A. Wing, A. Paytan, M. S. W. Hodgskiss, K. K. Mayfield, J. A. Hayles, J. E. Middleton, A.-S. C. Ahm, D. T. Johnston, F. Caxito, G. Uhlein, G. P. Halverson, B. Eickmann, M. Torres, T. J. Horner, Barium-isotopic constraints on the origin of post-Marinoan barites. *Earth Planet. Sci. Lett.* **519**, 234–244 (2019).
29. Y.-T. Hsieh, G. M. Henderson, Barium stable isotopes in the global ocean: Tracer of Ba inputs and utilization. *Earth Planet. Sci. Lett.* **473**, 269–278 (2017).
30. L. Bridgestock, Y.-T. Hsieh, D. Porcelli, W. B. Homoky, A. Bryan, G. M. Henderson, Controls on the barium isotope compositions of marine sediments. *Earth Planet. Sci. Lett.* **481**, 101–110 (2018).
31. Z. Cao, Y. Li, X. Rao, Y. Yu, E. C. Hathorne, C. Siebert, M. Dai, M. Frank, Constraining barium isotope fractionation in the upper water column of the South China Sea. *Geochim. Cosmochim. Acta* **288**, 120–137 (2020).
32. V. Mavromatis, K. van Zuilen, B. Purgstaller, A. Baldermann, T. F. Nägler, M. Dietzel, Barium isotope fractionation during witherite ($BaCO_3$) dissolution, precipitation and at equilibrium. *Geochim. Cosmochim. Acta* **190**, 72–84 (2016).
33. V. Mavromatis, K. van Zuilen, M. Blanchard, M. van Zuilen, M. Dietzel, J. Schott, Experimental and theoretical modelling of kinetic and equilibrium Ba isotope fractionation during calcite and aragonite precipitation. *Geochim. Cosmochim. Acta* **269**, 566–580 (2020).
34. B. M. Geyman, J. L. Ptacek, M. LaVigne, T. J. Horner, Barium in deep-sea bamboo corals: Phase associations, barium stable isotopes, & prospects for paleoceanography. *Earth Planet. Sci. Lett.* **525**, 115751 (2019).
35. Y.-B. Lin, H.-Z. Wei, F. Zhang, S. V. Hohl, G.-Y. Wei, T. Li, G.-L. Xiong, N. Li, S.-Y. Jiang, Evaluation of shallow-water corals and associated carbonate sediments as seawater Ba isotope archives in the South China Sea. *Palaeogeogr. Palaeoclimatol. Palaeoecol.* **605**, 111196 (2022).
36. A. Ridgwell, J. C. Hargreaves, N. R. Edwards, J. D. Annan, T. M. Lenton, R. Marsh, A. Yool, A. Watson, Marine geochemical data assimilation in an efficient Earth system model of global biogeochemical cycling. *Biogeosciences* **4**, 87–104 (2007).
37. K. Hans Wedepohl, The composition of the continental crust. *Geochim. Cosmochim. Acta* **59**, 1217–1232 (1995).
38. X.-Y. Nan, H.-M. Yu, R. L. Rudnick, R. M. Gaschnig, J. Xu, W.-Y. Li, Q. Zhang, Z.-D. Jin, X.-H. Li, F. Huang, Barium isotopic composition of the upper continental crust. *Geochim. Cosmochim. Acta* **233**, 33–49 (2018).
39. A. Reitz, K. Pfeifer, G. J. de Lange, J. Klump, Biogenic barium and the detrital Ba/Al ratio: A comparison of their direct and indirect determination. *Mar. Geol.* **204**, 289–300 (2004).
40. L. A. Melim, H. Westphal, P. K. Swart, G. P. Eberli, A. Munnecke, Questioning carbonate diagenetic paradigms: Evidence from the Neogene of the Bahamas. *Mar. Geol.* **185**, 27–53 (2002).
41. J. Veizer, A. Prokoph, Temperatures and oxygen isotopic composition of Phanerozoic oceans. *Earth Sci. Rev.* **146**, 92–104 (2015).
42. G.-Y. Wei, F. Zhang, Pristine or altered, what can early diagenesis tell us in shallow-water carbonates? *Earth Planet. Sci. Lett.* **641**, 118806 (2024).
43. S. B. Jacobsen, A. J. Kaufman, The Sr, C and O isotopic evolution of Neoproterozoic seawater. *Chem. Geol.* **161**, 37–57 (1999).
44. M. Elrick, J. F. Read, Cyclic ramp-to-basin carbonate deposits, cyclic ramp-to-basin carbonate deposits, Lower Mississippian, Wyoming and Montana; a combined field and computer modeling study. *J. Sediment. Res.* **61**, 1194–1224 (1991).
45. F. Martinez-Ruiz, A. Paytan, M. T. Gonzalez-Muñoz, F. Jroundi, M. M. Abad, P. J. Lam, J. K. B. Bishop, T. J. Horner, P. L. Morton, M. Kastner, Barite formation in the ocean: Origin of amorphous and crystalline precipitates. *Chem. Geol.* **511**, 441–451 (2019).
46. Z. Cao, C. Siebert, E. C. Hathorne, M. Dai, M. Frank, Constraining the oceanic barium cycle with stable barium isotopes. *Earth Planet. Sci. Lett.* **434**, 1–9 (2016).
47. S. L. Bates, K. R. Hendry, H. V. Pryer, C. W. Kinsley, K. M. Pyle, E. M. S. Woodward, T. J. Horner, Barium isotopes reveal role of ocean circulation on barium cycling in the Atlantic. *Geochim. Cosmochim. Acta* **204**, 286–299 (2017).
48. T. M. Lenton, M. Crouch, M. Johnson, N. Pires, L. Dolan, First plants cooled the Ordovician. *Nat. Geosci.* **5**, 86–89 (2012).
49. P. Maffre, Y. Godderis, A. Pohl, Y. Donnadieu, S. Carretier, G. Le Hir, The complex response of continental silicate rock weathering to the colonization of the continents by vascular plants in the Devonian. *Am. J. Sci.* **322**, 461–492 (2022).
50. J. P. Dunne, J. L. Sarmiento, A. Gnanadesikan, A synthesis of global particle export from the surface ocean and cycling through the ocean interior and on the seafloor. *Glob. Biogeochem. Cycles* **21**, GB4006 (2007).
51. L.-F. Gou, Z. Jin, A. Galy, Y.-Z. Gong, X.-Y. Nan, C. Jin, X.-D. Wang, J. Bouchez, H.-M. Cai, J.-B. Chen, H.-M. Yu, F. Huang, Seasonal riverine barium isotopic variation in the middle Yellow River: Sources and fractionation. *Earth Planet. Sci. Lett.* **531**, 115990 (2020).
52. A. Pohl, Z. Lu, W. Lu, R. G. Stockey, M. Elrick, M. Li, A. Desrochers, Y. Shen, R. He, S. Finnegan, A. Ridgwell, Vertical decoupling in Late Ordovician anoxia due to reorganization of ocean circulation. *Nat. Geosci.* **14**, 868–873 (2021).
53. D. O. Gough, "Solar interior structure and luminosity variations," in *Physics of Solar Variations*, V. Domingo, Ed. (Springer, 1981), pp. 21–34.
54. A. J. Krause, B. J. W. Mills, S. Zhang, N. J. Planavsky, T. M. Lenton, S. W. Poulton, Stepwise oxygenation of the Paleozoic atmosphere. *Nat. Commun.* **9**, 4081 (2018).
55. R. A. Berner, D. J. Beerling, R. Dudley, J. M. Robinson, R. A. Wildman, Phanerozoic atmospheric oxygen. *Annu. Rev. Earth Planet. Sci.* **31**, 105–134 (2003).
56. M. R. Saltzman, S. A. Young, L. R. Kump, B. C. Gill, T. W. Lyons, B. Runnegar, Pulse of atmospheric oxygen during the late Cambrian. *Proc. Natl. Acad. Sci. U.S.A.* **108**, 3876–3881 (2011).
57. F. Zhang, S. J. Romaniello, T. J. Algeo, K. V. Lau, M. E. Clapham, S. Richoz, A. D. Herrmann, H. Smith, M. Horacek, A. D. Anbar, Multiple episodes of extensive marine anoxia linked to global warming and continental weathering following the latest Permian mass extinction. *Sci. Adv.* **4**, e1602921 (2018).
58. H. C. Jenkyns, Geochemistry of oceanic anoxic events. *Geochem. Geophys. Geosyst.* **11**, Q03004 (2010).
59. M. R. Saltzman, Carbon and oxygen isotope stratigraphy of the Lower Mississippian (Kinderhookian–lower Osagean), western United States: Implications for seawater chemistry and glaciation. *Geol. Soc. Am. Bull.* **114**, 96–108 (2002).

60. C. R. Fielding, T. D. Frank, J. L. Isbell, *Resolving the Late Paleozoic Ice Age in Time and Space* (Geological Society of America, 2008), pp. 261–274.
61. M. V. Caputo, R. O. B. dos Santos, Stratigraphy and ages of four Early Silurian through Late Devonian, Early and Middle Mississippian glaciation events in the Parnaíba Basin and adjacent areas, NE Brazil. *Earth Sci. Rev.* **207**, 103002 (2020).
62. Y. Sun, M. M. Joachimski, P. B. Wignall, C. Yan, Y. Chen, H. Jiang, L. Wang, X. Lai, Lethally hot temperatures during the Early Triassic greenhouse. *Science* **338**, 366–370 (2012).
63. D. A. Katz, M. R. Buoniconti, I. P. Montañez, P. K. Swart, G. P. Eberli, L. B. Smith, Timing and local perturbations to the carbon pool in the lower Mississippian Madison Limestone, Montana and Wyoming. *Palaeogeogr. Palaeoclimatol. Palaeoecol.* **256**, 231–253 (2007).
64. M. R. Buoniconti, The evolution of the carbonate shelf margins and fill of the Antler foreland basin by prograding Mississippian carbonates, Northern U.S. Rockies, thesis, University of Miami (2018).
65. A. Paytan, Benthic Ba fluxes in the central Equatorial Pacific, implications for the oceanic Ba cycle. *Earth Planet. Sci. Lett.* **142**, 439–450 (1996).
66. B. A. Ward, J. D. Wilson, R. M. Death, F. M. Monteiro, A. Yool, A. Ridgwell, EcoGEnIE 1.0: Plankton ecology in the cGEnIE Earth system model. *Geosci. Model Dev.* **11**, 4241–4267 (2018).
67. D. Hülse, K. V. Lau, S. J. van de Velde, S. Arndt, K. M. Meyer, A. Ridgwell, End-Permian marine extinction due to temperature-driven nutrient recycling and euxinia. *Nat. Geosci.* **14**, 862–867 (2021).
68. A. Pohl, R. G. Stockey, X. Dai, R. Yohler, G. Le Hir, D. Hülse, A. Brayard, S. Finnegan, A. Ridgwell, Why the Early Paleozoic was intrinsically prone to marine extinction. *Sci. Adv.* **9**, eadg7679 (2023).
69. C. R. Scotese, N. Wright, PALEOMAP Paleodigital Elevation Models (PaleoDEMS) for the Phanerozoic (PALEOMAP Project, 2018); www.earthbyte.org/paleodem-resource-scotese-and-wright-2018/.
70. S. D. Schoepfer, J. Shen, H. Wei, R. V. Tyson, E. Ingall, T. J. Algeo, Total organic carbon, organic phosphorus, and biogenic barium fluxes as proxies for paleomarine productivity. *Earth Sci. Rev.* **149**, 23–52 (2015).

Acknowledgments: We thank P. Swart from the University of Miami for providing the SP samples. We thank the reviewers for the constructive comments, which have resulted in a much-improved and enhanced manuscript. **Funding:** This work was funded by the National Natural Science Foundation of China [42073002 (F.Z.)], the National Natural Science Foundation of China [42293280 (S.S.)], the U.S. National Science Foundation [EA-1733991 (M.E.)], the French Agence Nationale de la Recherche [ANR-22-CE01-0003 (project ECO-BOOST) and ANR-23-CE01-0003 (project CYCLO-SED) (A.P.)]. **Author contributions:** Conceptualization: F.Z. and S.S. Investigation: F.Z., A.P., M.E., G.-Y.W., K.C., P.C., M.F., Y.-B.L., N.L., X.W., and S.S. Methodology: F.Z., A.P., and Y.-B.L. Visualization: F.Z. and A.P. Writing—original draft: F.Z. Writing—review and editing: F.Z., A.P., M.E., G.-Y.W., K.C., P.C., M.F., Y.-B.L., N.L., X.W., and S.S. Resources: F.Z., A.P., M.E., and S.S. Funding acquisition: F.Z., A.P., M.E., and S.S. Data curation: F.Z. and A.P. Validation: F.Z., A.P., M.E., and S.S. Formal analysis: F.Z. and A.P. Software: F.Z. and A.P. Project administration: F.Z. **Competing interests:** The authors declare that they have no competing interests. **Data and materials availability:** The code for the version of the "muffin" release of the cGENIE Earth system model used in this paper is tagged as v0.9.62 and is assigned a DOI: https://zenodo.org/records/15073802. Configuration files for the specific experiments presented in the paper can be found in the directory: genie-userconfigs/PUBS/submitted/Zhang_et_al.PNAS.2023. Details of the experiments, plus the command line needed to run each one, are given in the README.txt file in that directory. Configuration files for the specific experiments presented in the paper can also be accessed using this link (https://zenodo.org/records/15369591). All other configuration files and boundary conditions are provided as part of the code release v0.9.62 (https://zenodo.org/records/15073802). A manual detailing code installation, basic model configuration, tutorials covering various aspects of model configuration, experimental design, and output, plus the processing of results, are assigned a DOI: https://zenodo.org/records/7545814. All data needed to evaluate the conclusions in the paper are present in the paper and/or the Supplementary Materials.

Submitted 12 December 2024
Accepted 22 May 2025
Published 2 July 2025
10.1126/sciadv.adv2756